

Automatic Detection of Atherosclerotic Plaque and Calcification From Intravascular Ultrasound Images by Using Deep Convolutional Neural Networks

Yi-Chen Li, Thau-Yun Shen¹, Chien-Cheng Chen¹, Wei-Ting Chang, Po-Yang Lee, and Chih-Chung Huang¹, *Senior Member, IEEE*

Abstract—Atherosclerosis is the major cause of cardiovascular diseases (CVDs). Intravascular ultrasound (IVUS) is a common imaging modality for diagnosing CVDs. However, an efficient analyzer for IVUS image segmentation is required for assisting cardiologists. In this study, an end-to-end deep-learning convolutional neural network was developed for automatically detecting media–adventitia borders, luminal regions, and calcified plaque in IVUS images. A total of 713 grayscale IVUS images from 18 patients were used as training data for the proposed deep-learning model. The model is constructed using the three modified U-Nets and combined with the concept of cascaded networks to prevent errors in the detection of calcification owing to the interference of pixels outside the plaque regions. Three loss functions (Dice, Tversky, and focal loss) with various characteristics were tested to determine the best setting for the proposed model. The efficacy of the deep-learning model was evaluated by analyzing precision–recall curve. The average precision (AP), Dice score coefficient, precision, sensitivity, and specificity of the predicted and ground truth results were then compared. All training processes were validated using leave-

one-subject-out cross-validation. The experimental results showed that the proposed deep-learning model exhibits high performance in segmenting the media–adventitia layers and luminal regions for all loss functions, with all tested metrics being higher than 0.90. For locating calcified tissues, the best result was obtained when the focal loss function was applied to the proposed model, with an AP of 0.73; however, the prediction efficacy was affected by the proportion of calcified tissues within the plaque region when the focal loss function was employed. Compared with commercial software, the proposed method exhibited high accuracy in segmenting IVUS images in some special cases, such as when shadow artifacts or side vessels surrounded the target vessel.

Index Terms—Atherosclerosis, convolutional neural network (CNN), deep learning, intravascular ultrasound (IVUS) imaging, plaque.

I. INTRODUCTION

HYPERTENSION, diabetes, and smoking are among the major risk factors of atherosclerosis, which is the main cause of cardiovascular diseases (CVDs). Atherosclerosis is the build-up of fats, cholesterol, and other substances and forms through a slow process. Over times, this plaque thickens the walls of arteries and narrows the luminal regions [1]. Therefore, intracoronary imaging of vessel wall structures is crucial for assessing plaque progression or regression during diagnosis, treatment, and prognosis [2]. Coronary angiography and intravascular ultrasound (IVUS) are common imaging modalities for coronary artery disease diagnosis. Angiography is the most commonly used method for intracoronary imaging using catheterization and is performed together with X-ray examination [3], which provides information on the luminal size of arteries but not on their structure or the composition of plaque [4]. IVUS is a valuable adjunct to angiography because it provides morphological and pathological information on arterial walls and plaque in real time [3]. Plaque burdens are located between the media–adventitia and luminal borders in the vessel wall. In general, the detection of media–adventitia borders is less difficult than that of luminal borders, because the media layer comprises smooth cells shown as a dark ring in IVUS images. By contrast, distinguishing the intima

Manuscript received December 22, 2020; accepted January 11, 2021. Date of publication January 18, 2021; date of current version April 26, 2021. This work was supported in part by the Show Chwan Memorial Hospital, Changhua, Taiwan, under Grant NCKUSCMH10805, in part by the National Health Research Institutes in Taiwan under Grant NHRI-EX107-10712EI, in part by the Ministry of Science and Technology of Taiwan under Grant MOST 107-2221-E-006-024-MY3, and in part by the Medical Device Innovation Center (MDIC), National Cheng Kung University (NCKU) from the Featured Areas Research Center Program within the framework of the Highest Education Sprout Project by the Ministry of Education (MoE) in Taiwan. (Yi-Chen Li and Thau-Yun Shen contributed equally to this work). (Corresponding author: Chih-Chung Huang.)

Yi-Chen Li and Po-Yang Lee are with the Department of Biomedical Engineering, National Cheng Kung University, Tainan 70101, Taiwan.

Thau-Yun Shen and Chien-Cheng Chen are with the Department of Cardiology, Show Chwan Memorial Hospital, Changhua 50008, Taiwan.

Wei-Ting Chang is with the Department of Cardiology, Chi-Mei Medical Center, Tainan 71004, Taiwan, also with the Institute of Clinical Medicine, College of Medicine, National Cheng Kung University, Tainan 70101, Taiwan, and also with the Department of Biotechnology, Southern Taiwan University of Science and Technology, Tainan 71005, Taiwan.

Chih-Chung Huang is with the Department of Biomedical Engineering, National Cheng Kung University, Tainan 70101, Taiwan, and also with the Medical Device Innovation Center, National Cheng Kung University, Tainan 70101, Taiwan (e-mail: cchuang@mail.ncku.edu.tw).

Digital Object Identifier 10.1109/TUFFC.2021.3052486

layer is slightly difficult because of greater scattering from erythrocytes within the lumen. Therefore, automatic estimation of the media–adventitia and luminal borders is essential for evaluating the degree of stenoses and luminal regions during IVUS-enabled diagnosis [4].

Typically, four plaque types—calcifications, necrotic cores, fibrous tissue, and fibro-fatty tissue—can be identified in an IVUS image [5]. Mintz [6] found that among these types of plaque, calcifications have a major impact on the progression and treatment of coronary diseases. Many intracoronary imaging studies have focused on the relationship between calcium and coronary atherosclerosis. The stable coronary lesions contain more calcium than unstable lesions. In addition, the amount of calcium may influence the treatment strategy and success of percutaneous coronary intervention [6]. Hence, automatic characterization of calcifications is required to assist in diagnosis and therapy. Current commercial IVUS imaging systems characterize plaque components using built-in software, such as virtual histology IVUS (VH-IVUS) (Philips Volcano Corporation, San Diego, CA, USA). In VH-IVUS, ultrasonic signals backscattered from the vessel wall are analyzed for characterizing plaque components [6], [8]. However, VH-IVUS is an offline software program and time-consuming to implement. In addition, VH-IVUS image frames are gated simultaneously using the R-wave of an electrocardiogram, and almost 96% of VH-IVUS image frames are discarded, decreasing the longitudinal resolution considerably [7]. Therefore, the use of built-in software (such as VH-IVUS) is not completely convenient in clinical operations, and image annotation must be performed manually by cardiologists or radiologists, which is a time-consuming process. Sometimes, interobserver and intraobserver variances occur during manual labeling. Therefore, many image-processing-based techniques have been developed over the past decade to identify media–adventitia layers and luminal regions in grayscale IVUS images. Katouzian *et al.* [4] summarized and categorized these approaches into several types, including edge-tracking [9]–[11], active-contour [12]–[14], probabilistic [15]–[17], and multiscale-expansion [18]–[20] techniques.

Owing to advances in hardware devices, artificial intelligence techniques have been proposed as an assistive tool in many medical image analysis applications, particularly in image segmentation obtained using machine or deep learning [7], [21], [28]. Several studies have used artificial intelligence techniques for IVUS image analysis. For instance, Taki *et al.* [7] implemented several texture analysis methods to extract hand-crafted features from IVUS images and classified the types of plaque by using a support vector machine and error-correcting output codes. Su *et al.* [21] adopted an artificial neural network with an autoencoder structure to segment media–adventitia layers and lumens in grayscale IVUS images through the use of imaged structural features. In both of these machine-learning-based studies, a manual feature-extraction procedure is required for model training. By contrast, deep learning automatically extracts image patterns without the need for feature extraction or user interaction. Yang *et al.* [28] employed a fully convolutional network for automatically delineating lumens and media–adventitia borders from images

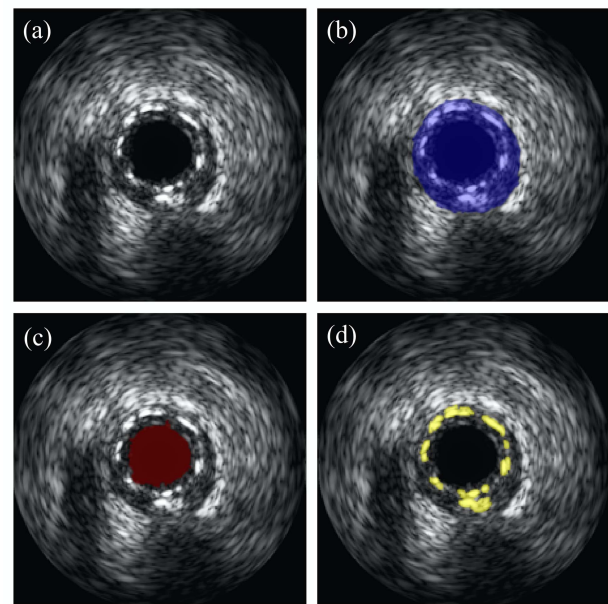


Fig. 1. Description of the IVUS image data set. (a) Typical original grayscale IVUS image, and corresponding manual annotations of the (b) region surrounded by the media–adventitia layer, (c) lumen region, and (d) locations of calcified tissues. The labeling was performed by cardiologists, and the annotations were used as the ground truth in this study.

in the publicly available IVUS database; however, plaque characterization was not performed.

Motivated by discussion on the characterization of plaque regions and the impact of calcified tissues, this study proposes an end-to-end deep-learning model consisting of three modified U-Nets to simultaneously segment media–adventitia layers and luminal regions and, most crucially, to locate calcified plaques in grayscale IVUS images. The U-Net architecture is adopted as the baseline of the proposed model on which the concept of cascaded networks is applied. Furthermore, this study evaluated different loss functions by applying them to imbalanced data to search for the prevailing factors in the proposed deep-learning approach for IVUS images.

II. MATERIALS AND METHODS

A. Image Acquisition and Preprocessing

Digital Imaging and Communications in Medicine (DICOM) IVUS images were acquired by Show Chwan Memorial Hospital, Taiwan, using an IVUS imaging system (Philips Volcano, Inc.) equipped with a solid-state IVUS transducer (with a synthetic aperture of 3.5 f and central frequency of 20 MHz; Eagle Eye Platinum ST, Philips Volcano, Inc.). Image markers and ring-down artifacts were removed before manual annotation to prevent detection errors. The entire data set contained 713 grayscale IVUS images obtained from 18 patients (56% men, 33% women, and 11% unknown). The annotation of arterial wall structures and calcium locations was performed by two cardiologists who were blinded to each patient's clinical situation. Three targets were annotated using Labelbox (Labelbox, San Francisco, CA, USA): the media–adventitia border, the luminal region, and calcium locations. Fig. 1 shows the manual annotations:

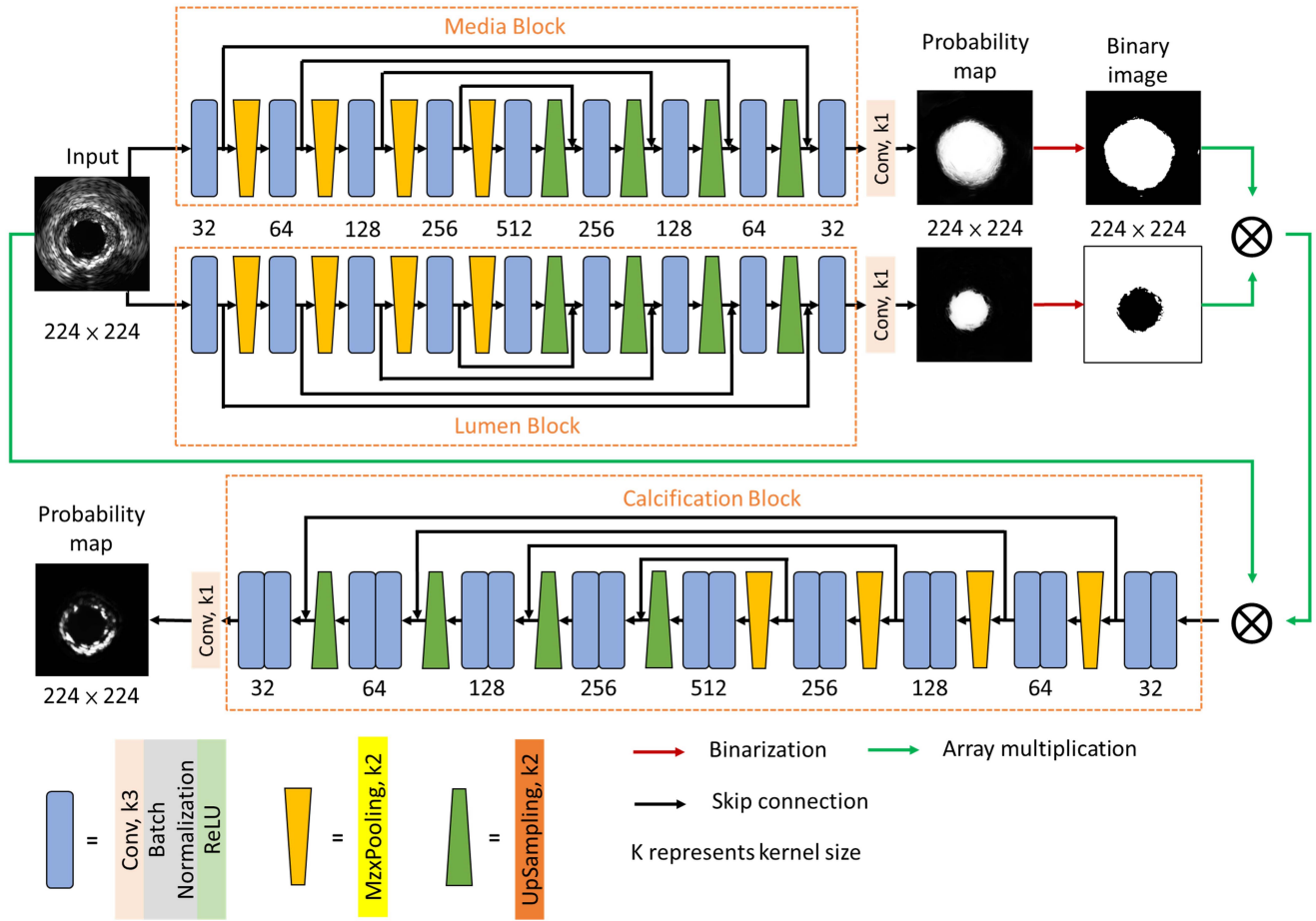


Fig. 2. Processes and detailed description of the proposed deep-learning CNN. The blocks and arrows denote the various operations: the blue block represents one convolution layer followed by a batch normalization layer and ReLU. The numbers (32, 64, 128, 256, etc.) are the kernel numbers in each convolution layer. K represents the kernel size. The number followed by K (e.g., $K1$) indicates the kernel size (1×1).

the original grayscale IVUS image [Fig. 1(a)]; the area surrounded by the media–adventitia layer, represented in blue [Fig. 1(b)]; the luminal region, represented in red [Fig. 1(c)]; and the location of calcified tissues inside the plaque region, represented in yellow [Fig. 1(d)]. All manual annotations were used as the ground truth for the proposed deep convolutional neural network (CNN). The size of the labels was identical to that of the original IVUS frames: 500×500 pixels. The pixel values of images and labels were normalized from $[0, 255]$ to $[0, 1]$ and resized to 224×224 to create the training data.

B. Deep-Learning Model

The overall process and details of the network are shown in Fig. 2. Detection of the media–adventitia, lumen, and calcium regions was performed by a deep CNN, which was inspired by the U-Net and cascaded network concept [24], [32]. This model was designed to have two stages. The first stage is the segmentation stage, denoted “Media Block” and “Lumen Block” in Fig. 2. In this stage, the plaque burden regions are extracted from the input images, which are connected directly to two CNNs with the same network architecture.

The architecture consists of multiple sets of layer operations. A layer operation contains one convolution operation with a kernel size of 3×3 and stride of 1, followed by a rectified linear unit (ReLU) and a batch normalization layer. The feature maps are downsampled to half the input resolution by the max pooling layer with a kernel size of 2×2 and stride of 2. After four-layer operations, the feature maps are upsampled by using transposed convolution with a kernel size of 2×2 and stride of 2. Subsequently, the feature maps are concatenated with the features obtained from the downsampled part. The concatenated feature maps are passed to the same operation layer as the downsampled part. In the final layer, the feature dimensions are reduced from 32 to 1 by using a convolution layer with a kernel size of 1×1 and sigmoid activation to arrange pixel-wise probabilities for each class. The outputs are called probability maps, and the pixel values are in the range 0–1. The networks in the first stage provide pixel-wise probabilities for the corresponding media–adventitia layers and lumen. These probability maps are transformed into binary masks using a predefined threshold, which was set to 0.1

$$ROI = \hat{P}_m \circ \hat{P}_l \quad (1)$$

$$X_{ROI} = ROI \circ X. \quad (2)$$

The media–adventitia and lumen masks are merged using (1), where \odot indicate the media–adventitia and lumen masks, respectively. The symbol \odot indicates the Hadamard product operation. The merged regions of interest (ROIs) are used only to preserve the plaque regions from the IVUS images. In (2), X represents the input IVUS image, which is obtained through the Hadamard product operation with the ROI masks consists of image information from only inside the plaque burden.

The second stage is the location stage, denoted “Calcification Block” in Fig. 2. In this stage, the network is used to locate calcified tissues inside the plaque burden X_{ROI} . The network architecture is similar to the one employed in the first stage except for the number of runs of the convolution operation in each layer operation. The layer operation consists of two convolutions followed by same-layer implementation. Three network structures are trained for each class simultaneously.

C. Loss Functions

The network is responsible for outputting probability maps for the training targets, and the loss functions are used to compute the difference between the ground truth masks and probability maps. This difference is then used to adapt the weighting by using the gradient descent between the network neurons. To determine the most effective loss function and ensure its convergence for the proposed deep-learning model, three loss functions were selected in this study owing to their ability to deal with class imbalance: Dice loss, Tversky loss, and focal loss.

1) **Dice Loss:** The Dice loss is the inverse of the Dice score coefficient (DSC), which is used to gauge the similarity between model prediction and ground truth. This function has been widely used in image segmentation tasks [33], [34]. The formulation of the Dice loss can be expressed as follows:

$$L_{\text{Dice}}(p, q) = 1 - 2 \frac{\sum_{n=1}^N p_n q_n + \varepsilon}{\sum_{n=1}^N (p_n + q_n) + \varepsilon} \quad (3)$$

where p and q represent the matrices of the probability map and ground truth mask, respectively; n and N refer to the positions of the pixels and the total number of pixels, respectively; and ε is a small constant to prevent the numerical issue of dividing by 0.

2) **Tversky Loss:** Tversky loss was proposed by Salehi *et al.* [35], and it can be expressed as follows:

$$L_{\text{Tversky}}(p, q; \alpha, \beta) = 1 - \frac{\sum_{n=1}^N p_n q_n + \varepsilon}{\sum_{n=1}^N p_n q_n + \alpha \sum_{n=1}^N (1 - p_n) q_n + \beta \sum_{n=1}^N p_n (1 - q_n) + \varepsilon} \quad (4)$$

where α and β are penalty-controlled weights to false positives (FPs) and false negatives (FNs), respectively, with $\alpha + \beta = 1$. The characteristic of this function is similar to that of the Dice loss; however, in the Dice loss, FPs and FNs have the same weight because the loss is the inverse of the DSC, which is the harmonic mean of precision and sensitivity. The Tversky loss emphasizes the effects on FPs and FNs in an imbalanced data

set and uses hyperparameters α and β to handle these issues. In this study, α and β were set to 0.3 and 0.7, respectively.

3) **Focal Loss:** The focal loss function is expressed as follows and is the modified pixel-wise cross-entropy loss for imbalanced image segmentation tasks [36]:

$$L_{\text{Focal}}(p, q; \omega, \gamma) = -\frac{1}{N} \sum_{n=1}^N \omega (1 - p_n)^\gamma q_n \log p_n + (1 - \omega) p_n^\gamma (1 - q_n) \log(1 - p_n). \quad (5)$$

In this function, to prevent the major background class or the easy training example from overwhelming the detector, the weighting factor ω and modulating factor $(1 - p_n)^\gamma$ are added to the cross-entropy. Additionally, ω is a predefined constant in the range $[0, 1]$; and $(1 - p_n)^\gamma$ is used to up-weight the hard classification examples, where the power γ is a focusing parameter in the range $[0, 5]$. In this study, ω was set to 0.25 and γ was set to 0.1 in accordance with the high performance of the proposed model compared with other hyperparameter settings.

D. Model Evaluation

The performance of the proposed model when using the three loss functions for IVUS application was evaluated by calculating the precision, sensitivity, specificity, and DSC. The numbers of true positives (TPs; correctly predicted foreground pixels), true negatives (TNs; correctly predicted background pixels), FPs (object pixels identified as the background), and FNs (background pixels but segmented as target objects) were obtained first from the confusion matrix.

Precision represents the ratio of the number of correctly predicted positive pixels to the total number of predicted positive pixels

$$\text{Precision} = \frac{\text{TP}}{\text{TP} + \text{FP}}. \quad (6)$$

Sensitivity, also known as recall, quantifies the proportion of the number of predicted positive values in the model to the correct number of positive values in the ground truth. Sensitivity is represented by

$$\text{Sensitivity} = \frac{\text{TP}}{\text{TP} + \text{FN}}. \quad (7)$$

Specificity is used to indicate the proportion of the number of predicted negative values in the segmentation model to the number of correct negative values in the ground truth. This evaluation metric is expressed as

$$\text{Specificity} = \frac{\text{TN}}{\text{TN} + \text{FP}}. \quad (8)$$

Because there was no calcified plaque in some of the IVUS images (in approximately 22% of the data acquired), some instances of zero division may have occurred. Therefore, we define the values of precision and sensitivity for this special condition.

- 1) When all the values of TPs, FPs, and FNs are 0 (indicating the absence of testing foreground and predicted foreground classes), the precision and sensitivity are both 1.

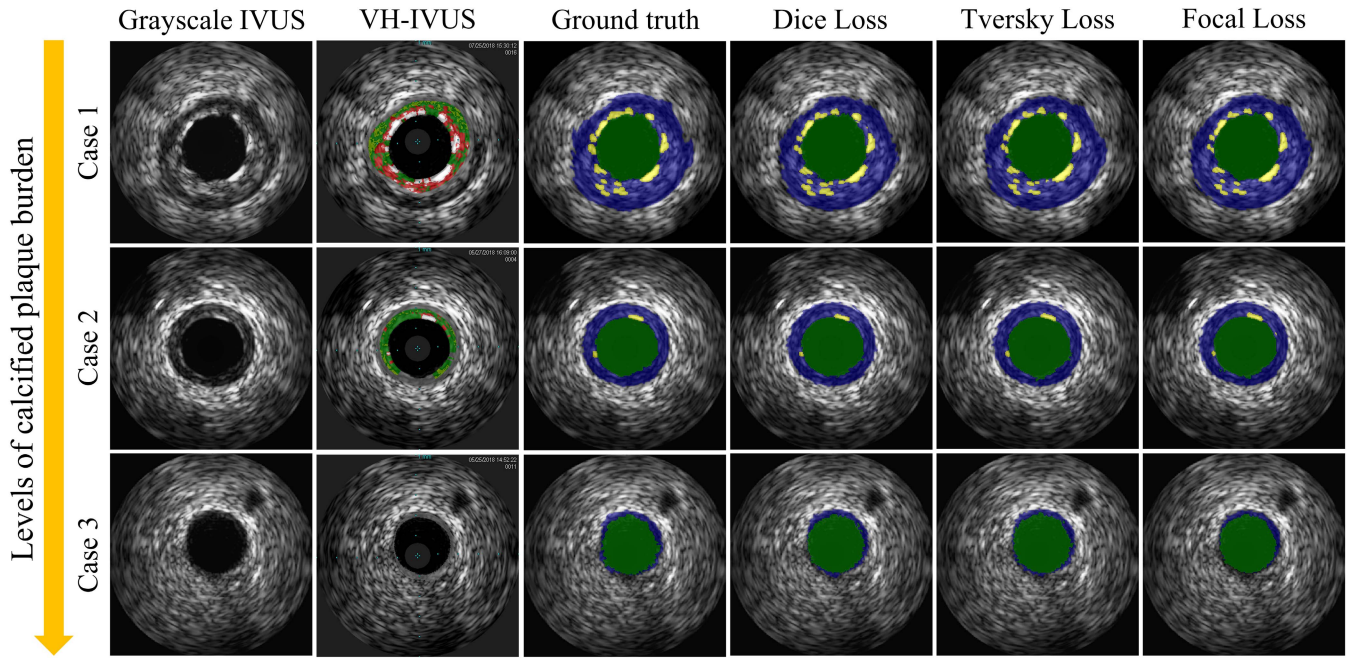


Fig. 3. Typical results of IVUS image segmentation performed using the proposed deep-learning method and different loss functions (Dice, Tversky, and focal loss) for three cases. The original grayscale IVUS images and their corresponding VH-IVUS images and ground truth images are also presented. In all images, except for the VH-IVUS images, green represents the luminal region, yellow indicates calcified tissue locations, and blue color represents other soft plaque burdens. Case 1 has the most calcified tissue, and Case 3 is a special condition wherein there is no calcified plaque burden on the vessel wall.

- 2) When the numbers of TPs and FPs are 0 (indicating the absence of a testing foreground class), the precision is 1 and the sensitivity is calculated using (7).
- 3) When the numbers of TPs and FNs are 0 (indicating the absence of a predicted foreground class), the precision is measured using (6) and the sensitivity is 1.

The specificity is directly calculated using (8) because this metric is unaffected by division by zero. The DSC gauges the degree of similarity between the output prediction and ground truth mask. This metric is evaluated using two mathematical sets X and Y , which indicate the predictive segmentation and ground truth, respectively. The metric can also be expressed in the form of the numbers of TPs, FPs, and FNs

$$\text{Dice score coefficient}(X, Y) = \frac{2|X \cap Y| + \varepsilon}{|X| + |Y| + \varepsilon} = \frac{2 * TP}{2 * TP + FP + FN}. \quad (9)$$

The DSC is in the range $[0, 1]$. If the predicted value is closer to the ground truth, the DSC is closer to 1. In addition, the precision–recall curve (PR curve) was analyzed and the average precision (AP) was obtained for comparing the segmentation performance of the model with the ground truth masks.

E. Training Strategy

The learning procedures when applying the various loss functions to the proposed CNN were all identical. The training images were shuffled and fed into the neural network at an image resolution of 224×224 pixels and batch size of 10 in each epoch. The Adam optimization method [37] was used in the training process with an initial learning rate of 0.01.

When the value of the validation loss had converged, the learning rate reduced by half, after which training was continued. The network with the lowest validation loss was preserved, and the output performance was computed with test images by using this network. Both stages performed training synchronously in this study, and the same loss functions were used in the first and second stage.

A leave-one-subject-out cross-validation approach was selected for validating the proposed CNN. In the data set, the images were separated on the basis of their subject so that no frame from the same subject appeared in another image group. This validation approach split the entire training process into n iterations, where n represented the number of subjects, which was 18 in this study. In each validation iteration, one image group was selected as the test set and the remaining 17 groups were selected as the training set. Eighteen deep-learning models were then trained and evaluated separately. The results were averaged to obtain the final test results.

F. Implementation

The deep-learning model was implemented using the open-source Tensorflow platform [38] version 1.9.0 in the Python programming language, version 2.7. The proposed model was trained under the configuration of eight NVidia Geforce GTX 1080Ti graphics cards (NVIDIA, USA), each with 11 GB of memory.

III. RESULTS

Fig. 3 shows three typical predicted results for IVUS images with predictions made by the proposed deep-learning model

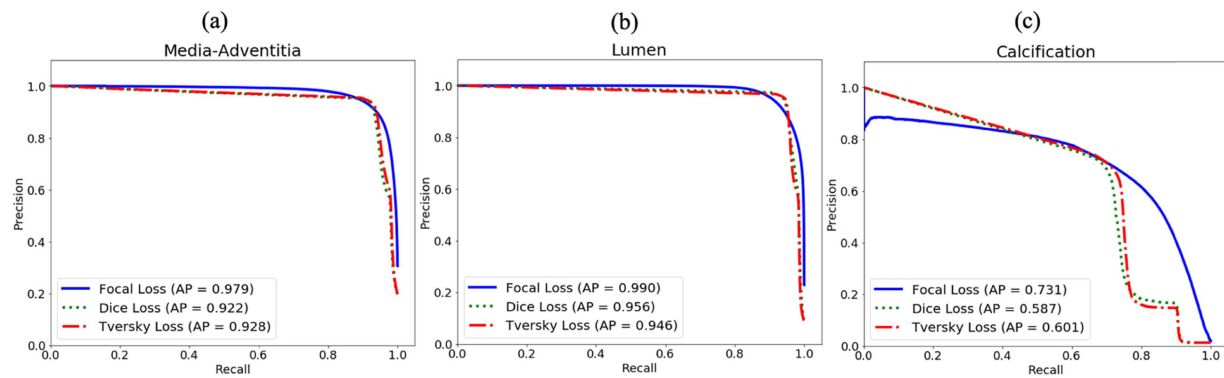


Fig. 4. Comparison of the PR curves for testing the efficacy of the proposed method with different loss functions (Dice, Tversky, and focal loss): segmentation results for (a) media-adventitia region, (b) lumen region, and (c) calcified tissue locations.

TABLE I

QUANTITATIVE INDEXES OF MEDIA-ADVENTITIA, LUMEN, AND CALCIFICATION SEGMENTATIONS USING THE PROPOSED DEEP-LEARNING METHOD WITH VARIOUS LOSS FUNCTIONS (DICE, TVERSKY, AND FOCAL LOSS). THE RESULTS ARE PRESENTED AS THE MEAN \pm STANDARD DEVIATION

<i>Dice Loss</i>					
	DSC	Precision	Sensitivity	Specificity	AP
media-adventitia	0.93 \pm 0.04	0.94 \pm 0.06	0.93 \pm 0.05	0.99 \pm 0.01	0.92 \pm 0.06
Lumen	0.95 \pm 0.02	0.95 \pm 0.03	0.95 \pm 0.03	0.99 \pm 0.01	0.96 \pm 0.03
Calcification	0.65 \pm 0.18	0.74 \pm 0.21	0.75 \pm 0.11	0.99 \pm 0.01	0.59 \pm 0.26
<i>Tversky Loss</i>					
	DSC	Precision	Sensitivity	Specificity	AP
media-adventitia	0.93 \pm 0.04	0.93 \pm 0.06	0.94 \pm 0.01	0.99 \pm 0.01	0.93 \pm 0.05
Lumen	0.95 \pm 0.03	0.94 \pm 0.03	0.96 \pm 0.02	0.99 \pm 0.01	0.95 \pm 0.04
Calcification	0.66 \pm 0.17	0.72 \pm 0.18	0.77 \pm 0.08	0.99 \pm 0.01	0.60 \pm 0.25
<i>Focal Loss</i>					
	DSC	Precision	Sensitivity	Specificity	AP
media-adventitia	0.93 \pm 0.03	0.95 \pm 0.03	0.93 \pm 0.04	0.99 \pm 0.01	0.98 \pm 0.02
Lumen	0.95 \pm 0.02	0.95 \pm 0.02	0.95 \pm 0.02	0.99 \pm 0.01	0.99 \pm 0.01
Calcification	0.67 \pm 0.15	0.77 \pm 0.15	0.72 \pm 0.09	0.99 \pm 0.01	0.73 \pm 0.26

with the three loss functions. The figure shows the ground truth masks and VH-IVUS images. All images except for the grayscale IVUS and VH-IVUS images were color-coded: green (luminal region), yellow (locations of calcified plaque burden), and blue (other soft tissues in the plaque region). Each case (Cases 1–3) shows a different calcified plaque burden. Case 1 exhibits the most calcified plaque, which is located around the lumen. The amount of calcified plaque tissue in Case 2 is less than that in Case 1. Case 3 is a special condition in which no calcifications or any other lesions exist on the arterial walls. Each case belongs to a different subject. The media-adventitia layers and lumen were accurately detected from the images using the proposed deep-learning model with various loss functions. Most crucially, the proposed deep-learning model precisely labeled the calcified tissues even though the amounts of coronary calcification varied considerably. However, for some of the VH-IVUS images, such as for Case 1, errors were made regarding the media-adventitia layer, influencing the calcification classification. In fact, the images of Case 3 in Fig. 3 are the “poor” IVUS images from the clinician’s point of view. Because the variations of gray-level between media-adventitia border and

surrounding tissue are similar to each other compared to them in Cases 1 and 2, which makes the segmentation more difficult.

The PR curves for image segmentations performed using the Dice loss, Tversky loss, and focal loss after 18 iterations of training of the proposed deep-learning model with leave-one-subject-out cross-validation are shown in Fig. 4; the curves were constructed by averaging all 18 PR curves from each training iteration, and the AP was computed from the PR curves. The proposed model achieved an AP of more than 0.95 in the detection of both media-adventitia layer and lumen regions for all loss functions, as illustrated in Fig. 4(a) and (b). However, the APs obtained using the proposed model and the Dice loss (0.587) and Tversky loss (0.601) were slightly lower than the APs obtained using the proposed model with the focal loss (0.731) in calcification detection, as shown in Fig. 4(c).

Quantitative analysis of the proposed deep-learning model for IVUS image segmentation is summarized in Table I. The measured indexes were the DSC, precision, sensitivity, specificity, and AP. The results are presented as the mean \pm standard deviation of all measurements. In the detection of media-adventitia layer and luminal regions, most metrics (DSC, precision, sensitivity, and specificity) were higher than

TABLE II

QUANTITATIVE INDEXES OF MEDIA-ADVENTITIA, LUMEN, AND CALCIFICATION SEGMENTATION USING THE PROPOSED DEEP-LEARNING METHOD WITH VARIOUS LOSS FUNCTIONS (DICE, TVERSKY, AND FOCAL LOSS) FOR DIFFERENT PROPORTIONS OF CALCIFIED TISSUE WITHIN THE PLAQUE REGION. THE RESULTS ARE PRESENTED AS THE MEAN \pm STANDARD DEVIATION

		<i>Dice Loss</i>				<i>Tversky Loss</i>				<i>Focal Loss</i>			
		DSC	Prec.	Sen.	Spec.	DSC	Prec.	Sen.	Spec.	DSC	Prec.	Sen.	Spec.
0%~10%	Media-Adven	0.92 \pm	0.90 \pm	0.96 \pm	0.98 \pm	0.92 \pm	0.89 \pm	0.96 \pm	0.98 \pm	0.93 \pm	0.93 \pm	0.94 \pm	0.99 \pm
	titia	0.08	0.13	0.07	0.02	0.09	0.14	0.06	0.02	0.06	0.10	0.06	0.02
	Lumen	0.95 \pm	0.94 \pm	0.95 \pm	0.99 \pm	0.95 \pm	0.93 \pm	0.96 \pm	0.99 \pm	0.95 \pm	0.95 \pm	0.95 \pm	0.99 \pm
		0.05	0.06	0.06	0.01	0.05	0.06	0.05	0.01	0.04	0.05	0.06	0.01
	Calcification	0.55 \pm	0.62 \pm	0.81 \pm	0.99 \pm	0.53 \pm	0.58 \pm	0.80 \pm	0.99 \pm	0.59 \pm	0.71 \pm	0.72 \pm	0.99 \pm
		0.39	0.41	0.27	0.01	0.40	0.41	0.29	0.01	0.39	0.38	0.34	0.01
Over 10%~30 %	Media-Adven	0.93 \pm	0.96 \pm	0.91 \pm	0.99 \pm	0.94 \pm	0.95 \pm	0.93 \pm	0.99 \pm	0.93 \pm	0.96 \pm	0.91 \pm	0.99 \pm
	titia	0.05	0.06	0.09	0.01	0.05	0.07	0.08	0.01	0.06	0.04	0.09	0.01
	Lumen	0.96 \pm	0.96 \pm	0.95 \pm	0.99 \pm	0.96 \pm	0.96 \pm	0.95 \pm	0.99 \pm	0.96 \pm	0.96 \pm	0.95 \pm	0.99 \pm
		0.04	0.05	0.05	0.01	0.04	0.05	0.06	0.01	0.03	0.04	0.05	0.01
	Calcification	0.76 \pm	0.83 \pm	0.74 \pm	0.99 \pm	0.77 \pm	0.82 \pm	0.77 \pm	0.99 \pm	0.74 \pm	0.84 \pm	0.71 \pm	0.99 \pm
		0.20	0.17	0.22	0.01	0.18	0.17	0.20	0.01	0.22	0.16	0.24	0.01
Over 30 %	Media-Adven	0.93 \pm	0.96 \pm	0.91 \pm	0.99 \pm	0.93 \pm	0.94 \pm	0.92 \pm	0.99 \pm	0.94 \pm	0.96 \pm	0.92 \pm	0.99 \pm
	titia	0.04	0.06	0.06	0.02	0.04	0.06	0.06	0.02	0.04	0.05	0.06	0.01
	Lumen	0.95 \pm	0.99 \pm	0.92 \pm	0.99 \pm	0.95 \pm	0.98 \pm	0.92 \pm	0.99 \pm	0.95 \pm	0.97 \pm	0.93 \pm	0.99 \pm
		0.03	0.01	0.06	0.01	0.03	0.01	0.06	0.01	0.03	0.03	0.06	0.01
	Calcification	0.81 \pm	0.88 \pm	0.75 \pm	0.99 \pm	0.82 \pm	0.88 \pm	0.79 \pm	0.99 \pm	0.84 \pm	0.88 \pm	0.81 \pm	0.99 \pm
		0.09	0.07	0.12	0.01	0.10	0.07	0.15	0.01	0.09	0.07	0.14	0.01

Prec.: Precision, Sen.: Sensitivity, Spec.: Specificity

0.93 with a standard deviation of lower than 0.06. The DSC, precision, sensitivity, and AP for locating the calcified tissues inside plaque regions were lower than those for detecting media-adventitia layer and luminal regions. All the values for specificity were 0.99 ± 0.01 , because the computation employed the predictive negatives as the baseline to obtain the diagnostic ability for true background pixels (the numerator and denominator are similar).

Because the proportion of calcified tissues within the plaque region may affect calcified plaque detection, we tested the deep learning model with different amounts of calcification in the plaque region (Table II). Before testing, the proportion of calcified tissues in the plaque region was computed for each image. The calcified proportions, ranging from 0% to 40%, were split into three levels: 0% to 10%, >10% and $\leq 30\%$, and >30%. The DSC, precision, sensitivity, and specificity values for detecting media-adventitia layer and luminal regions were

still higher than 0.90 for the three loss functions in all cases. The average DSC and precision for locating the calcified tissues increased with the proportion of calcified tissues for all loss functions, which implied that a higher proportion of calcification resulted in higher accuracy of the proposed model.

VH-IVUS is a standard software program for analyzing IVUS images in clinical applications. However, VH-IVUS results sometimes confuse cardiologists, particularly when the image contains shadow artifacts or other side vessels. Fig. 5 shows two cases as an example; the original grayscale IVUS images, ground truth images, VH-IVUS images, and the image results from the proposed deep-learning model when using the focal loss are compared. The proposed model still provides a more accurate prediction of the media-adventitia border, lumen region, and locations of calcified plaque than VH-IVUS, with which incorrect detections were made when

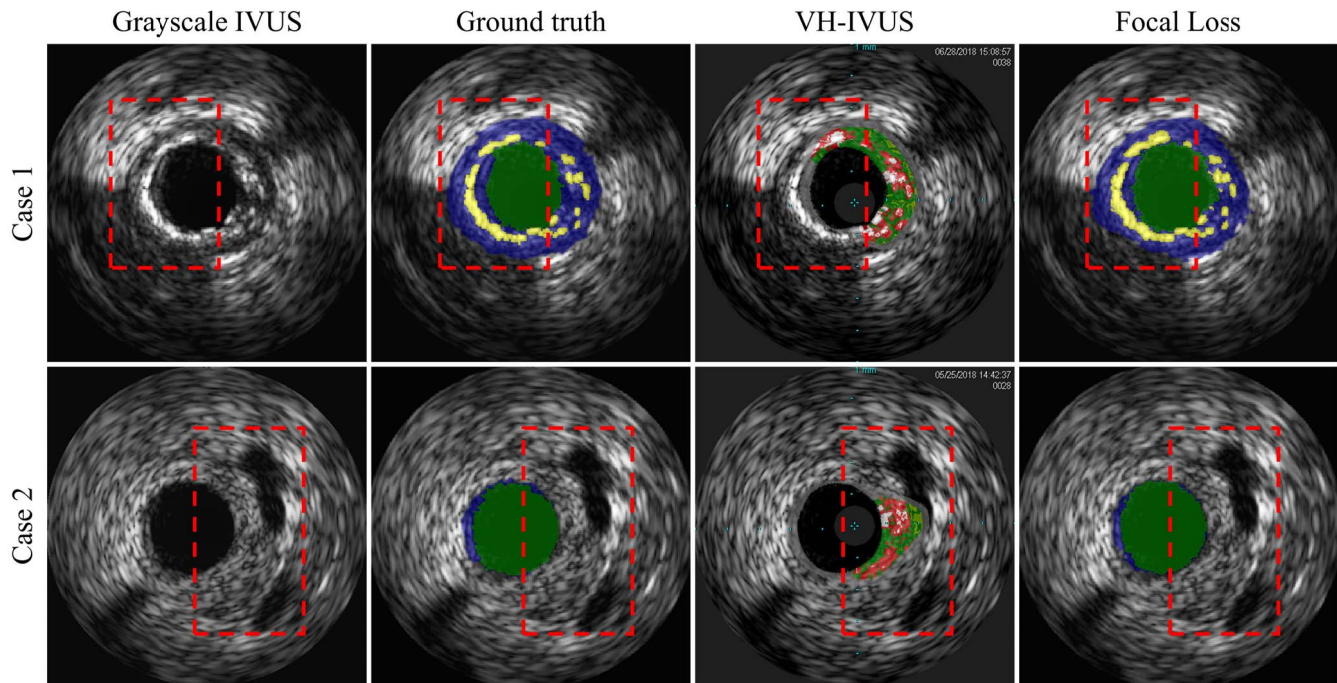


Fig. 5. Visual segmentation results for two special conditions. In Case 1, the dotted red rectangles indicate the region of a shadow artifact, where VH-IVUS incorrectly detected a media–adventitia layer and calcification. In Case 2, the dotted red rectangles indicate the regions in which side vessels were incorrectly detected by VH-IVUS.

the IVUS image contained artifacts, such as the shadow region in Case 1 and side vessels in Case 2.

IV. DISCUSSION

Arterial wall detection and plaque characterization play an essential role in the clinical diagnosis of CVDs. Although the commercial software VH-IVUS has a plaque characterization function, its offline implementation, low longitudinal resolution, and errors such as those illustrated in Fig. 3 (Case 1) and Fig. 5 mean that cardiologists must spend considerable time in manual labeling. Therefore, in this study, we proposed a deep-learning model for the automatic analysis of IVUS images to assist cardiologists. The automated segmentation of calcified tissue remains a challenge owing to the varying amounts and complicated distributions of such tissue. In this study, an automatic method was proposed for segmenting media–adventitia layers, luminal regions, and calcified tissues by using three CNNs. In the proposed method, two stages are employed to prevent bright speckle noise outside the plaque region from being detected during segmentation of the calcified tissue locations. In the first stage, the probability maps of the media–adventitia and lumen classes are output. After binarization, these results are used to extract the ROI as the input to the second stage; this prevents the stage of calcified tissue identification from being affected by interference from pixels outside the plaque region. In the second stage, the probability maps of the calcification class are output. The major difference between these stages is that the number of convolution operations in the location stage is more than that in the segmentation stage. This design was used on the basis of our experimental experience regarding the hyperparameters

of convolutional layers and makes the proposed method better than an architecture constructed using triple standard U-Nets. In other words, more feature information is required for locating calcified tissues owing to their complex shapes and distributions. By contrast, for segmenting media–adventitia layers and luminal regions, small-scale features are required to achieve high accuracy because their image structures are similar and around the center of the image.

Based on this two-stage CNN design, deep learning was shown to be suitable for IVUS image analysis (Fig. 3). Fig. 3 shows three cases of IVUS images showing different amounts of calcified tissue; the predicted images from the proposed model were similar to the ground truth mask images when using different loss functions for all cases. In fact, the loss function plays an important role in deep learning. Therefore, three loss functions were tested in this study. The PR curves obtained using the proposed model when detecting the media–adventitia layers, luminal regions, and calcified tissues with different loss functions are shown in Fig. 4. The higher the AP, the higher the performance of the deep-learning model. All loss functions resulted in high AP (>0.92) when segmenting the media–adventitia layers [Fig. 4(a)] and luminal regions [Fig. 4(b)]; however, the model exhibited superior results for calcification detection when the focal loss function was employed (AP of 0.73) than one of the other two loss functions was used. This result is in favorable agreement with all other values listed in Table I. All the values are higher than 0.93 in the detection of media–adventitia layers and luminal regions; however, the values are lower for calcification detection. Again, the model obtained superior results when the focal loss function was used (mean DSC of 0.67, precision of 0.77,

sensitivity of 0.72, specificity of 0.99, and AP of 0.73 were obtained using the focal loss in calcification detection). The focal loss is a type of loss modified from cross-entropy and focuses on pixel-wise performance to ensure that the output probability maps are close to 0 or 1 (negatives or positives). It combines additional penalty terms such as weighting and modulation factors to enhance the affection of imbalanced class, and these terms make the training process prone to convergence within a hundred epochs. Therefore, the focal loss is recommended for application to the proposed deep-learning model for classifying IVUS images.

The proportion of calcified tissues within the plaque region affects calcified plaque detection. The detection of media–adventitia layers and luminal regions by using the proposed deep-learning model was unaffected by the calcification effect, even when there was no calcified plaque on the arterial walls. However, it is clear that small amounts of calcified burden can lower the prediction accuracy of the proposed model (Table II). The DSC and precision increased with the proportion of calcified tissues for all three loss functions. For example, when the focal loss was applied to the deep-learning model, the DSC was 0.59 when the proportion of calcified tissues was less than 10%; this value increased to 0.84 when the calcified tissues comprised more than 30% of the entire plaque region. Calcified plaque usually exhibits high echogenicity in grayscale ultrasound images; however, because the proportion of calcification is low in the entire plaque region, the speckle features may not be sufficiently clear for distinguishing between the different plaque types. Therefore, the model's predictions were influenced by the proportion of calcified tissue.

If image artifacts or side vessels exist, VH-IVUS is prone to errors when segmenting an IVUS image, as illustrated in Fig. 5. In VH-IVUS, the frequency domain information of ultrasound signals backscattered from tissues is analyzed. The backscattered signals may be easily influenced by plaque or vessel wall structures, as shown in Fig. 5 (Case 1), in which a shadow artifact resulting from arcs calcification is present (dotted red window). Because calcified tissues appear as bright regions like the adventitia layer, VH-IVUS incorrectly detects the inner border of calcified tissue as media–adventitia layer. For Case 2 in Fig. 5 (dotted red window), apart from the target vessel, side vessels are included in the IVUS image. VH-IVUS was affected by the signals inside the lumens of side vessels because in this image, a small amount of plaque is shown on the arterial wall, and the intima and media layers cannot be clearly observed. This condition also leads to incorrect detection of the media–adventitia layer and luminal region because of unclear borders in the grayscale image. However, the proposed deep-learning model still had high accuracy in the classification of IVUS images in these special cases.

Su *et al.* [21] used an artificial neural network for lumen and MA border detection in IVUS images. The experimental results showed that the Jaccard index is about 0.92 and 0.91 for lumen and MA detection in IVUS testing data, respectively. Yang *et al.* [28] used a fully convolutional network for segmenting lumen and MA border automatically in IVUS images. The Jaccard measures are about 0.90 and 0.86 for lumen and

MA segmentation, respectively. Balakrishna *et al.* [39] also used an U-net with VGG16 encoders to detect the lumen and MA automatically in IVUS images, and the results showed that the best measurements of Dice coefficient are about both 0.88 for lumen and MA, respectively. All above state-of-the-art models showed that the similarities between artificial intelligence and manual operation are about 0.88 and 0.92 in lumen and MA detection. However, no calcification detection was performed in the above studies, and the DSCs of lumen and MA segmentation are about 0.95 and 0.93 as the focal loss was applied on IVUS image in this study.

V. CONCLUSION

In this study, an end-to-end deep-learning model was proposed for automatically detecting media–adventitia borders, luminal regions, and calcified plaque in IVUS images. To the best of our knowledge, the proposed model is the first of its kind to employ CNNs for locating calcified tissues in grayscale IVUS images. The proposed model uses the standard U-Net architecture as the baseline and incorporates the concept of cascaded networks to prevent incorrect identification of calcification outside the plaque burden. Unlike other machine-learning models, which require preprocessing of IVUS images, the proposed deep-learning model can directly analyze a raw DICOM image from Philips machine with electrical scan. Three loss functions—Dice loss, Tversky loss, and focal loss—were tested to determine the best setting for the proposed model for IVUS image segmentation. The performance of the deep-learning model was evaluated using data obtained from 18 patients by calculating several metrics: PR curve, AP, DSC, precision, sensitivity, and specificity. The qualitative and quantitative results demonstrated that the proposed model performed most highly when the focal loss function was employed for the IVUS image segmentation task. In addition, compared with commercial software, the proposed method exhibited high accuracy in the segmentation of IVUS images in some special cases, such as when shadow artifacts or side vessels surrounded the target vessel in images.

REFERENCES

- [1] J. Sanz and Z. A. Fayad, "Imaging of atherosclerotic cardiovascular disease," *Nature*, vol. 451, no. 7181, pp. 953–957, Feb. 2008.
- [2] R. Fedewa *et al.*, "Artificial intelligence in intracoronary imaging," *Current Cardiol. Rep.*, vol. 22, no. 7, p. 46, Jul. 2020.
- [3] S. E. Nissen and P. Yock, "Intravascular ultrasound: Novel pathophysiological insights and current clinical applications," *Circulation*, vol. 103, no. 4, pp. 604–616, Jan. 2001.
- [4] A. Katouzian, E. D. Angelini, S. G. Carlier, J. S. Suri, N. Navab, and A. F. Laine, "A state-of-the-art review on segmentation algorithms in intravascular ultrasound (IVUS) images," *IEEE Trans. Inf. Technol. Biomed.*, vol. 16, no. 5, pp. 823–834, Sep. 2012.
- [5] L. S. Athanasiou, D. I. Fotiadis, and L. K. Michalis, *Atherosclerotic Plaque Characterization Methods Based on Coronary Imaging*. New York, NY, USA: Academic, 2017.
- [6] G. S. Mintz, "Intravascular imaging of coronary calcification and its clinical implications," *JACC, Cardiovascular Imag.*, vol. 8, no. 4, pp. 461–471, Apr. 2015.
- [7] A. Taki, A. Roodaki, S. K. Setarehdan, S. Avansari, G. Unal, and N. Navab, "An IVUS image-based approach for improvement of coronary plaque characterization," *Comput. Biol. Med.*, vol. 43, no. 4, pp. 268–280, May 2013.

- [8] A. Nair, B. D. Kuban, E. M. Tuzcu, P. Schoenhagen, S. E. Nissen, and D. G. Vince, "Coronary plaque classification with intravascular ultrasound radiofrequency data analysis," *Circulation*, vol. 106, no. 17, pp. 2200–2206, Oct. 2002.
- [9] M. Sonka *et al.*, "Segmentation of intravascular ultrasound images: A knowledge-based approach," *IEEE Trans. Med. Imag.*, vol. 14, no. 4, pp. 719–732, Dec. 1995.
- [10] C. von Birgelen *et al.*, "Morphometric analysis in three-dimensional intracoronary ultrasound: An *in vitro* and *in vivo* study performed with a novel system for the contour detection of lumen and plaque," *Amer. Heart J.*, vol. 132, no. 3, pp. 516–527, Sep. 1996.
- [11] W. Li *et al.*, "Semi-automatic contour detection for volumetric quantification of intracoronary ultrasound," in *Proc. Comput. Cardiol.*, Sep. 1994, pp. 277–280.
- [12] D. Gil and P. Radeva, "A regularized curvature flow designed for a selective shape restoration," *IEEE Trans. Image Process.*, vol. 13, no. 11, pp. 1444–1458, Nov. 2004.
- [13] M. E. Plissiti, D. I. Fotiadis, L. K. Michalis, and G. E. Bozios, "An automated method for lumen and media-adventitia border detection in a sequence of IVUS frames," *IEEE Trans. Inf. Technol. Biomed.*, vol. 8, no. 2, pp. 131–141, Jun. 2004.
- [14] Y. Zhu and Z. Yan, "Computerized tumor boundary detection using a Hopfield neural network," *IEEE Trans. Med. Imag.*, vol. 16, no. 1, pp. 55–67, Feb. 1997.
- [15] E. Brusseau, C. L. deKorte, F. Mastik, J. Schaar, and A. F. W. vanderSteen, "Fully automatic luminal contour segmentation in intracoronary ultrasound imaging—A statistical approach," *IEEE Trans. Med. Imag.*, vol. 23, no. 5, pp. 554–566, May 2004.
- [16] A. Taki *et al.*, "Automatic segmentation of calcified plaques and vessel borders in IVUS images," *Int. J. Comput. Assist. Radiol. Surg.*, vol. 3, nos. 3–4, pp. 347–354, Sep. 2008.
- [17] M.-H.-R. Cardinal, J. Meunier, G. Soulez, R. L. Maurice, E. Therasse, and G. Cloutier, "Intravascular ultrasound image segmentation: A three-dimensional fast-marching method based on gray level distributions," *IEEE Trans. Med. Imag.*, vol. 25, no. 5, pp. 590–601, May 2006.
- [18] A. Katouzian, B. Baseri, E. E. Konofagou, and A. F. Laine, "Automatic detection of blood versus non-blood regions on intravascular ultrasound (IVUS) images using wavelet packet signatures," *Proc. SPIE*, vol. 6920, Mar. 2008, Art. no. 69200H.
- [19] A. Katouzian, E. Angelini, A. Lersakul, B. Sturm, and A. F. Laine, "Lumen border detection of intravascular ultrasound via denoising of directional wavelet representations," in *Proc. Int. Conf. Funct. Imag. Modeling Heart*. Paris, France: Springer, 2009, pp. 104–113.
- [20] A. Katouzian, E. D. Angelini, B. Sturm, and A. F. Laine, "Automatic detection of luminal borders in IVUS images by magnitude-phase histograms of complex brushlet coefficients," in *Proc. Annu. Int. Conf. IEEE Eng. Med. Biol.*, Aug. 2010, pp. 3073–3076.
- [21] S. Su, Z. Hu, Q. Lin, W. K. Hau, Z. Gao, and H. Zhang, "An artificial neural network method for lumen and media-adventitia border detection in IVUS," *Comput. Med. Imag. Graph.*, vol. 57, pp. 29–39, Apr. 2017.
- [22] J. Long, E. Shelhamer, and T. Darrell, "Fully convolutional networks for semantic segmentation," in *Proc. IEEE Conf. Comput. Vis. Pattern Recognit.*, Jun. 2015, pp. 3431–3440.
- [23] H. Noh, S. Hong, and B. Han, "Learning deconvolution network for semantic segmentation," in *Proc. IEEE Int. Conf. Comput. Vis.*, Dec. 2015, pp. 1520–1528.
- [24] O. Ronneberger, P. Fischer, and T. Brox, "U-Net: Convolutional networks for biomedical image segmentation," in *Proc. Int. Conf. Med. Image Comput. Comput.-Assist. Intervent.* Berlin, Germany: Springer, 2015, pp. 234–241.
- [25] D. Li *et al.*, "Parallel deep neural networks for endoscopic OCT image segmentation," *Biomed. Opt. Exp.*, vol. 10, no. 3, pp. 1126–1135, 2019.
- [26] Y. Zhao *et al.*, "Knowledge-aided convolutional neural network for small organ segmentation," *IEEE J. Biomed. Health Inform.*, vol. 23, no. 4, pp. 1363–1373, Jul. 2019.
- [27] P. F. Christ *et al.*, "Automatic liver and tumor segmentation of CT and MRI volumes using cascaded fully convolutional neural networks," 2017, *arXiv:1702.05970*. [Online]. Available: <http://arxiv.org/abs/1702.05970>
- [28] J. Yang, L. Tong, M. Faraji, and A. Basu, "IVUS-Net: An intravascular ultrasound segmentation network," in *Proc. Int. Conf. Smart Multimedia*. Paris, France: Springer, 2018, pp. 367–377.
- [29] C. Szegedy *et al.*, "Going deeper with convolutions," in *Proc. IEEE Conf. Comput. Vis. Pattern Recognit.*, Jun. 2015, pp. 1–9.
- [30] M. Z. Alom, M. Hasan, C. Yakopcic, T. M. Taha, and V. K. Asari, "Recurrent residual convolutional neural network based on U-Net (R2U-Net) for medical image segmentation," 2018, *arXiv:1802.06955*. [Online]. Available: <http://arxiv.org/abs/1802.06955>
- [31] K. Zhang *et al.*, "Zebrafish embryo vessel segmentation using a novel dual ResUNet model," *Comput. Intell. Neurosci.*, vol. 2019, pp. 1–14, Feb. 2019.
- [32] P. F. Christ *et al.*, "Automatic liver and lesion segmentation in CT using cascaded fully convolutional neural networks and 3D conditional random fields," in *Proc. Int. Conf. Med. Image Comput. Comput.-Assist. Intervent.* Greece: Springer, 2016, pp. 415–423.
- [33] L. Baskaran *et al.*, "Identification and quantification of cardiovascular structures from CCTA: An end-to-end, rapid, pixel-wise, deep-learning method," *JACC, Cardiovascular Imag.*, vol. 13, no. 5, pp. 1163–1171, 2020.
- [34] S. Aslani *et al.*, "Multi-branch convolutional neural network for multiple sclerosis lesion segmentation," *Neuroimage*, vol. 196, pp. 1–15, Aug. 2019.
- [35] S. S. M. Salehi, D. Erdogmus, and A. Gholipour, "Tversky loss function for image segmentation using 3D fully convolutional deep networks," in *Proc. Int. Workshop Mach. Learn. Med. Imag.* Toronto, ON, Canada: Springer, 2017, pp. 379–387.
- [36] T.-Y. Lin, P. Goyal, R. Girshick, K. He, and P. Dollár, "Focal loss for dense object detection," in *Proc. IEEE Int. Conf. Comput. Vis.*, Oct. 2017, pp. 2980–2988.
- [37] D. P. Kingma and J. Ba, "Adam: A method for stochastic optimization," 2014, *arXiv:1412.6980*. [Online]. Available: <http://arxiv.org/abs/1412.6980>
- [38] M. Abadi *et al.*, "Tensorflow: A system for large-scale machine learning," in *Proc. 12th USENIX Symp. Operating Syst. Design Implement. (OSDI)*, 2016, pp. 265–283.
- [39] C. Balakrishna, S. Dadashzadeh, and S. Soltaninejad, "Automatic detection of lumen and media in the IVUS images using U-Net with VGG16 encoder," 2018, *arXiv:1806.07554*. [Online]. Available: <http://arxiv.org/abs/1806.07554>



Yi-Chen Li was born in Kaohsiung, Taiwan. She received the B.S and M.S. degrees in biomedical engineering from National Cheng Kung University, Tainan, Taiwan, in 2018 and 2020, respectively.

Her interests include the imaging processing of ultrasound imaging and image segmentation with machine learning and deep learning.



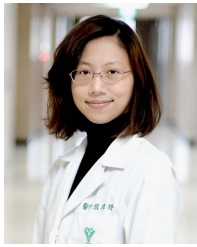
Thau-Yun Shen was born in 1968. He received the medical degree with National Yang-Ming University, Taipei, Taiwan, in 1993.

He completed cardiovascular training with Shun-Tian General Hospital, Taichung, Taiwan. He is currently the Director with Cardiology Department, Show Chwan Memorial Hospital, Changhua, Taiwan, where he is also the Interventional Cardiologist.



Chien-Cheng Chen was born in 1965. He received the medical degree with the China Medical College, Taichung, Taiwan, in 1991.

He completed cardiovascular training with Mackay Memorial Hospital, Taipei, Taiwan. He was the Director with the Cardiology Department, Show Chwan Memorial Hospital, Changhua, China. He is currently the Medical Secretary and the Deputy Principal of Medical Vice Superintendent with the Show Chwan Memorial Hospital.



Wei-Ting Chang was born in Hsinchu, Taiwan, in 1982. She received the medical degree with National Cheng Kung University and Hospital, Tainan, Taiwan, in 2007.

She completed cardiovascular training with National Cheng Kung University and Hospital in 2012. More than a cardiologist, she has enthusiasm on basic science and has been as a Research Fellow with the Harvard Medical School, Boston, MA, USA, and Brigham and Women's Hospital, Boston, from 2013 to 2014.

As back in Taiwan, she established "Circulation Lab" with the Chi-Mei Medical Center, Tainan, Taiwan, and focused on researches of translational medicine, echocardiography, cardio-oncology, and pulmonary hypertension. She has authored more than 90 SCI articles.

Dr. Chang was honored with Ta-You Wu Memorial Award for her outstanding work in 2017.



Po-Yang Lee was born in Taipei, Taiwan. He received the B.S. degree in electronic engineering from Ming Chuan University, Taipei, in 2009, and the M.S. degree in electrical engineering from Fu Jen Catholic University, New Taipei City, Taiwan, in 2014. He is currently pursuing the Ph.D. degree in biomedical engineering with National Cheng Kung University, Tainan, Taiwan.

From 2017 to 2018, he worked as a Research Trainee with the Department of Physiology and Biomedical Engineering, Mayo Clinic, Rochester, MN, USA. He is a co-founder of Ficuson Tech, Taiwan. His research interests include the development of high-frequency ultrasound imaging system, point-of-care ultrasonic system, and ultrasound beamforming method with deep learning.



Chih-Chung Huang (Senior Member, IEEE) was born in Taoyuan, Taiwan. He received the B.S., M.S., and Ph.D. degrees in biomedical engineering from Chung Yuan Christian University, Chung-Li, Taiwan, in 2002, 2003, and 2007, respectively.

From 2006 to 2007, he worked at the NIH Resource Center for Medical Ultrasonic Transducer Technology, University of Southern California, Los Angeles, CA, USA as a Visiting Researcher, where he was engaged in research of high-frequency ultrasound imaging and development of new acoustic methods for cataract diagnosis. In 2008, he joined the Department of Electrical Engineering, Fu Jen Catholic University, New Taipei City, Taiwan, as an Assistant Professor. In 2012, he was promoted as an Associate Professor. In 2013, he joined the Department of Biomedical Engineering, National Cheng Kung University, Tainan, Taiwan. He is currently a Professor at the Department of Biomedical Engineering. He was the Deputy Director of the Medical Device Innovation Center, the Deputy Director of the Technology Transfer and Business Incubation Center, the Strategic Planning Division Director of the Research and Services Headquarters at National Cheng Kung University. His research interests include ultrasonic tissue characterization, blood flow measurement, high frequency ultrasound, and ultrasonic instrument for medical applications, etc.

Dr. Huang was selected as a member of IFMBE Asia-Pacific Research Networking Fellowship as well as the ordinary member of CoS representative of Taiwanese Society of Biomedical Engineering of IFMBE affiliated Society. He was the Secretary General of Taiwanese Society of Biomedical Engineering. He is an Associate Editor of the *Medical Physics* and the *Journal of Medical and Biological Engineering*. He is the TPC Member of the IEEE IUS.